

# The Role of Alloying Elements on the Crevice Corrosion Behavior of Ni-Cr-Mo Alloys

N. Ebrahimi,<sup>‡\*</sup> P. Jakupi,<sup>\*</sup> J.J. Noël,<sup>\*</sup> and D.W. Shoesmith<sup>\*</sup>

## ABSTRACT

The roles of the alloying elements Mo, Cr, and W in resisting crevice corrosion of UNS N06022, UNS N06625, and UNS N10362 have been studied under galvanostatic conditions in 5 mol/L NaCl at 150°C. Corrosion damage patterns were investigated using surface analytical techniques such as scanning electron microscopy and optical imaging, and the corrosion products characterized by energy dispersive x-ray spectroscopy. While the Cr content of the alloy is critical in controlling initiation of crevice corrosion, the rate of activation (passive-to-active transition) is influenced by both the Cr and the Mo (and W) contents. The alloy's Mo content also determines the distribution of corrosion damage within the crevice. In alloys with high Mo content, corrosion propagates laterally across the surface, while in alloys with low Mo content, it penetrates into the alloy. This can be attributed to the accumulation of molybdates (and tungstates), which stifle alloy dissolution at active sites. Thus, as the Mo content of the alloy increases in the order N06625 (9 wt% Mo) < N06022 (13 wt% Mo [3 wt% W]) < N10362 (22 wt% Mo), the depth of corrosion penetration decreases. In addition, once crevice corrosion initiates and the crevice acidifies, metal oxidation can also couple to proton reduction inside the crevice. The role of internal proton reduction in driving the crevice corrosion of these Ni alloys was found to be quite significant; greater than 50% of the corrosion damage is caused by proton reduction inside the crevice.

**KEY WORDS:** crevice corrosion, galvanostatic polarization, molybdenum, Ni-Cr-Mo alloys

## INTRODUCTION

Extensive industrial effort has been invested in the design of nickel superalloys able to resist corrosion in aggressive media. This is generally achieved by alloying Ni with various amounts of Cr and Mo, along with small amounts of other alloying elements such as W, Cu, and Fe.<sup>1</sup> Mo is known to enhance the corrosion resistance in reducing conditions, while Cr is a beneficial element under oxidizing conditions.<sup>2-3</sup> While the properties of the oxides that protect these alloys generally enforce good passive corrosion behavior, the function of individual alloying elements in resisting localized corrosion processes, in particular pitting and crevice corrosion, is not fully understood, and optimization of alloy composition for corrosion reliability and cost has not yet been achieved.

Ni-Cr-Mo alloys show a great resistance to general corrosion,<sup>3</sup> but under aggressive conditions they can suffer localized corrosion, such as pitting and crevice corrosion. The effects of many factors, such as temperature, pH, and the presence of aggressive halides, on the crevice corrosion of these alloys have been studied, and in general the susceptibility to crevice corrosion was found to increase when the temperature and chloride concentration were increased.<sup>4-7</sup> Generally, the localized corrosion performance of passive metals and alloys is assured by aggressive electrochemical testing, and a wide range of Ni-Cr-Mo alloys have been investigated.

Many researchers have investigated the role of alloying elements on the localized corrosion of Ni alloys.<sup>8-10</sup> To date, studies have shown that Cr is the

Submitted for publication: July 14, 2015. Revised and accepted: September 6, 2015. Preprint available online: September 7, 2015. <http://dx.doi.org/10.5006/1848>.

<sup>‡</sup> Corresponding author. E-mail: nebrahi6@uwo.ca.

<sup>\*</sup> Department of Chemistry and Surface Science Western, The University of Western Ontario, London, Ontario, Canada.

primary alloying element for maintaining passivity.<sup>11-17</sup> Lloyd, et al.,<sup>11,18</sup> studied the passive behavior in acidic solutions of five Ni-Cr-Mo alloys with varying amounts of Cr and Mo, and found much lower passive dissolution currents, and a much slower attainment of steady-state passive conditions, on those alloys with >20% Cr content.

Kehler and Scully<sup>19-20</sup> found that the rate of occurrence of metastable corrosion events in acidic solution increased with a decrease in alloy Mo content. Studies in simulated crevice solutions on a series of Ni-Cr-Mo alloys performed by Lillard, et al.,<sup>21</sup> showed that, as the Mo content of the alloy increased, the passive current density and the dissolution rate associated with the active region decreased. A decrease in crevice corrosion rate resulting from an increase in Mo content has also been reported.<sup>22</sup>

Many other studies have also focused on the role of Mo in corrosion behavior of Ni-based alloys.<sup>23-25</sup> Mishra, et al.,<sup>26</sup> studied the effects of Cr, Mo, and W on the crevice corrosion of a number of commercial Ni-Cr-Mo(-W) alloys in 1.0 mol/L sodium chloride and demonstrated the synergistic influence of Cr and Mo in controlling passive film breakdown. The "protection temperature" was used to rank the resistance of these alloys to crevice corrosion, and the following ranking was achieved: high Cr + low Mo < low Cr + high Mo < high Cr + high Mo < high Cr + high (Mo + W).

While these studies<sup>26-27</sup> yield little mechanistic information, an alloy's resistance to localized corrosion is generally attributed to the quality and composition of the passive film and how this is influenced by alloy composition and microstructure. A combination of electrochemical impedance spectroscopy and x-ray photoelectron spectroscopy (XPS) measurements on the C22 alloy<sup>†</sup> (UNS N06022),<sup>(1)</sup> in neutral pH solution and at different applied potentials, showed that the resistance of the oxide film ( $R_{\text{film}}$ ) is controlled by its  $\text{Cr}_2\text{O}_3$  content, and that once the transpassive potential region is reached,  $R_{\text{film}}$  decreases, accompanied by a dramatic increase in the  $\text{Cr}(\text{OH})_3$  content of the film.<sup>28</sup> A later XPS and time-of-flight secondary ion mass spectrometry (ToF-SIMS) study on the same system showed that transpassive dissolution is accompanied by the accumulation of Mo(VI) and W(VI) species in the outer region of the film.<sup>29</sup> More recently, Zhang, et al.,<sup>29-31</sup> studied the properties of the oxide film on Ni-Cr-Mo alloys as a function of applied potential, temperature, and pH using various surface analytical techniques, such as angle-resolved XPS, synchrotron radiation XPS, ToF-SIMS, and scanning electron microscopy (SEM). The presence of a layered structure in the passive film (<5 nm) was demonstrated, with an inner  $\text{Cr}_2\text{O}_3$  layer, outer Cr/Ni

hydroxides, and Mo/Cu or Mo/W oxide in the outermost surface.

Once the passive film breaks down and stable propagation is established, the role of alloying elements in repassivation of the crevice becomes important. Published studies have indicated a role for Mo in determining the crevice propagation rate.<sup>9,21</sup> Jakupi, et al.,<sup>32</sup> studied the crevice corrosion of UNS N06022 under galvanostatic polarization, and suggested that propagation was controlled by the Mo content, and the damage distribution depended on a combination of applied current and the deposition of Mo-containing solids. Enrichment of corrosion products comprising O, Mo, and W was also reported by Shan, et al., suggesting that propagation is controlled by the deposition of Mo and W.<sup>10</sup>

The goal of this research is to expand on previous studies by investigating three commercial alloys with various Cr and Mo contents in an attempt to confirm that Cr and Mo work synergistically to control crevice corrosion susceptibility and propagation.<sup>26</sup> The authors' main interests are in the passive-to-active transition and the propagation process, in particular the distribution of corrosion damage and how it is influenced by the composition of the alloy. To achieve this goal, crevice corrosion was driven galvanostatically, to guarantee initiation and also to prevent repassivation. In this manner one can isolate the propagation stage and control the total amount of corrosion damage.

## EXPERIMENTAL PROCEDURES

The compositions of the alloys used in this study are listed in Table 1. All alloys were supplied by Haynes International<sup>†</sup>. The specimens were machined and bent into a V-shape to produce an artificial crevice assembly containing only one crevice. The crevice electrode design has been described elsewhere.<sup>32-34</sup> A 0.8 mm thick PTFE slice was used as a crevice former to produce a crevice with an area of ~4 cm<sup>2</sup>. The area of uncreviced material exposed to solution was ~10.5 cm<sup>2</sup>. Each sample was wet-ground with silicon carbide paper from a 180 to a 1200 grit finish, ultrasonically cleaned in methanol, and rinsed in ultra-pure deionized water. Before tightening the crevice assembly, the metal electrode and the PTFE crevice former were immersed in the electrolyte solution to ensure the presence of electrolyte in the crevice interior. All tests were performed at 150°C in a 5 M NaCl solution. The solutions were prepared from reagent grade NaCl and Type-I water (resistivity of 18.2 MΩ · cm<sup>2</sup>) obtained from a Milli-Q Academic A-10<sup>†</sup> system. A new solution was used for each experiment.

### Electrochemical Cell

All of the crevice corrosion experiments were conducted inside a cylindrical pressure vessel with a

<sup>†</sup> Trade name.

<sup>(1)</sup> UNS numbers are listed in *Metals and Alloys in the Unified Numbering System*, published by the Society of Automotive Engineers (SAE International) and cosponsored by ASTM International.

**TABLE 1**  
Chemical Composition (wt%) of Alloys N06022, N10362, and N06625

Alloy/Element	Ni	Cr	Mo	W	Fe	Co	C	Mn	S	Si
UNS N06022	56	22	13	3	3	2.5	0.01	0.5	0.02	0.08
UNS N10362	62	15	22	–	2	–	0.01	0.25	–	0.08
UNS N06625	62	21	9	–	5	1	0.10	0.5	–	0.5

100 mm inner diameter and a volume of 1,000 cm<sup>3</sup>. The working electrode was suspended near the center of the cell using a cylindrical rod of the same material from which the crevice was formed. The rod was connected to a tapped hole in one end of the creviced electrode. To avoid galvanic corrosion, the counter electrode was made from the same material as the crevice. To mimic the usual crevice corrosion geometry, the surface area of the counter electrode was much larger than that of the creviced electrode. The reference electrode was a homemade Ag/AgCl electrode in a saturated KCl solution.<sup>35</sup> Before and after each experiment, its potential was checked against a saturated calomel electrode that was used only as a reference electrode, and the difference was always  $-45 \pm 3$  mV.

For each experiment, 500 cm<sup>3</sup> of electrolyte solution was air saturated by agitation in air. The sealed assembly was then pressurized with 400 kPa of ultra-high purity Ar gas (Praxair<sup>†</sup>) to ensure proper sealing of the pressure vessel. In this study, two galvanostatic currents, 10  $\mu$ A and 200  $\mu$ A, were applied to the working electrode at 150°C and the crevice potential ( $E_C$ ) response measured using an a WaveDrive 20 Bipotentiostat<sup>†</sup> (Pine Instruments).

### Analyses of Corroded Electrodes

After the experiment, the creviced electrodes were washed with deionized water, rinsed with ethanol, and dried using Ar gas. The crevice corroded surface and depth of corrosion propagation were then examined by optical microscopy, SEM, and energy-dispersive x-ray spectroscopy (EDS).

A LEO (Zeiss) 1540XB<sup>†</sup> FIB/SEM was used for imaging in secondary and backscatter modes and a beam energy of 10 KeV was used for all EDS analyses.

To measure the depth of corrosion penetration, the sample was polished from the edge of the sample toward the center of the corroded area until the center was reached. Image analysis software (Image Pro Plus<sup>†</sup>) was used to measure the total damaged area within the crevice and also the maximum depth of crevice penetration. EDS was used to determine the composition of the corrosion products on the corroded surface and to map the corrosion front on a cross-sectioned crevice.

A series of BC1<sup>†</sup> (UNS N10362) alloy specimens were weighed before and after corrosion. Weight loss (W) measurements were performed after corrosion that was forced by a constant applied charge ( $Q_A$ , the applied current multiplied by the time for which it was

applied). The dark-colored, gel-like corrosion products were removed by wiping immediately on completing the experiment. The specimen was then rinsed with water and ultrasonically cleaned in ethanol for 5 min, and then dried in ultra high purity Ar. The working electrode was dried in the desiccator for 1 d before being weighed. An uncertainty in W arises from the fact that some corrosion products that segregated to grain boundaries could not be removed by this method, which leads to an underestimation of W.

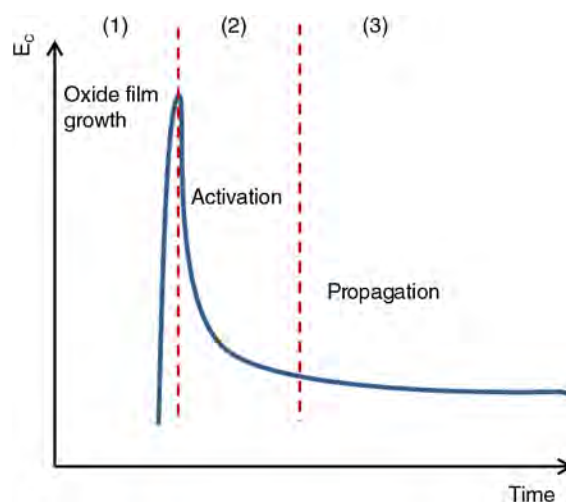
A 10 mL volume of the solution, sampled after the corrosion experiment, was analyzed by inductively-coupled plasma mass spectrometry (ICP-MS) to measure the amounts of dissolved Cr, Mo, and Ni in the solution. The detection limit was 0.2  $\mu$ g/L for dissolved Mo and Cr and, for Ni, 0.001  $\mu$ g/L.

## RESULTS

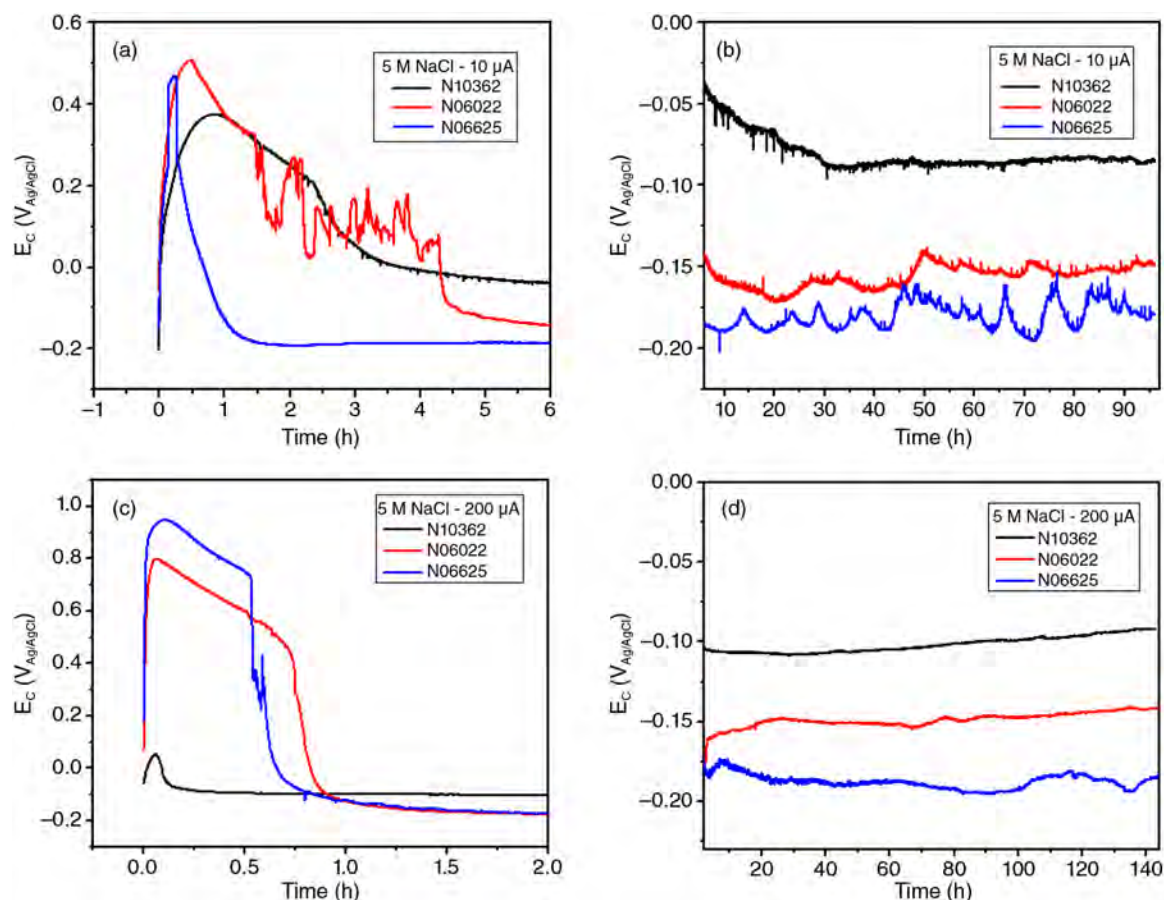
### Crevice Corrosion under Galvanostatic Conditions

Figure 1 shows a schematic illustration of the  $E_C$  response of an alloy on application of a constant current. Three distinct stages are observed:

1. At short times  $E_C$  increases with time as the applied current forces the anodic growth of the passive oxide film.
2.  $E_C$  reaches a maximum and then decreases as locations within the creviced area activate.
3. Propagation



**FIGURE 1.** Schematic of the  $E_C$ -time response to an applied current showing the three distinct regions of anodic oxide film growth (Stage 1), crevice activation (Stage 2), and crevice propagation (Stage 3).



**FIGURE 2.**  $E_C$ -time for the three alloys: (a) and (b) under galvanostatic polarization at  $10 \mu\text{A}$ , and (c) and (d) under galvanostatic polarization at  $200 \mu\text{A}$ .

3.  $E_C$  achieves an approximately steady-state value indicating the establishment of active propagation conditions within the crevice. The activation stage (Stage 2) represents the period required to establish a sufficiently large IR drop and critical crevice solution<sup>36-37</sup> to place the creviced locations in an active region.<sup>38</sup>

Figures 2(a) and (b) show the measured  $E_C$  for currents of  $10 \mu\text{A}$ , applied for 4 d, and  $200 \mu\text{A}$ , applied for 6 d, for the three alloys. A previous study<sup>32</sup> showed that a minimum current of  $10 \mu\text{A}$  was needed to initiate crevice corrosion in a crevice of the same geometry on the N06022 alloy at  $120^\circ\text{C}$ . Therefore, the  $10 \mu\text{A}$  current was chosen to study the stages involved in the transition from passive to active behavior. At the higher current, this transition was rapid and the electrode was in the active propagation stage for the majority of the experiment.

In Stage 1,  $E_C$  rose rapidly and at an effectively identical rate for the two high-Cr alloys (N06022 and N06625) and to a higher value than for the low-Cr alloy (N10362). Although only a qualitative feature, this increase illustrated the more rapid growth of the Cr(III) oxide barrier layer associated with passivity on the high-Cr alloys.<sup>39</sup> The slower rise in

$E_C$ , and lower potential threshold for the onset of activation, for the N10362 alloy could then be attributed to its lower Cr content. At the higher applied current, the difference in behavior between the high- and low-Cr alloys in Stage 1 became distinctly more marked. A considerably higher potential threshold was observed for the N06022 and N06625 alloys, and that for the N10362 alloy was significantly reduced. While the absolute value of  $E_C$  had no particular significance, the comparative effect was consistent with the influence of Cr content on breakdown potentials.<sup>26</sup>

The activation pattern (Stage 2) also varied with alloy composition and applied current (Figure 2). As expected, the time required to complete activation was shorter at the higher applied current (Figure 2[c]) and predominantly determined by Cr content, being completed in ~45 min to 1 h for the high-Cr alloys, but almost instantaneously for the low-Cr-containing N10362 alloy. Passivity was not established on the N10362 alloy prior to the activation of crevice corrosion.

At the lower applied current, however, activation occurred much more slowly, and the time required to complete the activation process was not directly related to the Cr content of the alloy. Despite the high Cr

content, activation occurred in 1 h on the N06625 alloy with a Mo content of only 9 wt%. For the N10362 alloy, activation required 3 h to 4 h despite the significantly lower Cr content, showing that once the Cr(III) oxide layer was breached, the establishment of active crevice propagation conditions was predominantly controlled by the Mo content. Closer inspection of the  $E_C$ -time plot for the N10362 alloy during the activation stage detected minor negative-going transients (not shown in Figure 2[a]), which are typical of metastable film-breakdown/repair events.<sup>40</sup> As noted previously,<sup>20,23</sup> such transients have been attributed to the suppression by Mo of breakdown events that lead to establishment of active crevice sites. While the very high Mo content could suppress these minor metastable events, it could not prevent eventual activation at such a low Cr content.

For the N06022 alloy, the passive-to-active transition was not so readily achieved, and major fluctuations occurred, the alloy apparently making a number of major attempts to activate before finally achieving the fully activated state. Because the Cr and Mo contents are inverted in this alloy compared to those in the N10362 alloy (Table 1), this behavior was consistent with an improved ability to resist film breakdown, resulting from the high Cr content, but a lower ability to resist activation, resulting from the lower Mo (or Mo + W) content. The competition between these two processes results in a slightly longer period to complete activation on N06022 than on the N10362 alloy.

Once active corrosion was fully established (Stage 3),  $E_C$  achieved an approximately steady-state value for all three alloys (Figures 2[b] and [d]). As shown in Figure 3, the average  $E_C$  ( $\pm\sigma$ ) over the propagation time in Stage 3 was proportional to the Mo content of the alloy, but only slightly dependent on the applied current. This suggests that the chemistry in active

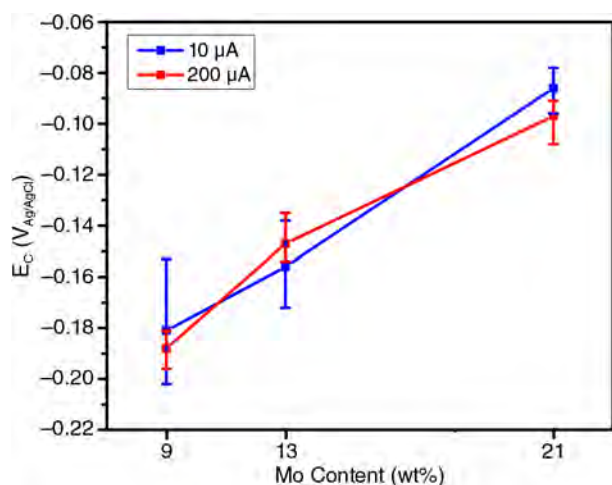


**FIGURE 3.**  $E_C$  as a function of alloy Mo content for crevice corrosion with applied currents of 10  $\mu$ A and 200  $\mu$ A: the range shows the average, maximum, and minimum  $E_C$  at each current.

locations within the crevice was controlled predominantly by Mo. Although, when determined using an external reference electrode, the value of  $E_C$  measured is the potential outside the crevice mouth; it is influenced by the potential achieved at the active locations within the crevice. Thus, the increasingly positive  $E_C$  observed (for the same applied current) as the alloy Mo content increased indicated that active conditions were more difficult to sustain on alloys with high Mo content, consistent with the expectation that Mo will suppress the active dissolution rates. The lack of dependence of  $E_C$  on applied current indicates that the active corrosion process is not solely driven by the externally applied current but is also dependent on other reactions occurring inside the crevice. The important role of internal crevice reactions has been noted before in the crevice corrosion of titanium,<sup>35,41</sup> with a large fraction of corrosion being driven by internal proton reduction leading to hydrogen evolution.

Both the absolute value of, and the fluctuations in,  $E_C$  were dependent, in amplitude and frequency, on the Mo content (Figure 2[d]). A possible explanation for this behavior is that the fluctuations indicated the propagation of active corrosion within freshly exposed (activated) sites, which would exhibit a low  $E_C$ , with the eventual rise in  $E_C$  indicating the build-up of Mo at those locations. Such a process would be rapid for the high-Mo N10362 alloy, on which  $E_C$  was steady, but slower for low-Mo N06625, on which  $E_C$  fluctuated significantly.

### Energy-Dispersive X-Ray Spectroscopy and Scanning Electron Microscopy Analyses

Figure 4 shows an optical image of the corroded surface of the N10362 alloy after corrosion at an applied current of 200  $\mu$ A, and the stained PTFE crevice former removed from it. As expected, the crevice initiated near the edge (crevice mouth) and propagated both along the edge and into the creviced region. Beyond the actively corroded area, the majority of the uncorroded creviced area was stained by acid, and probably also some redeposited corrosion products that diffused out of the active area.

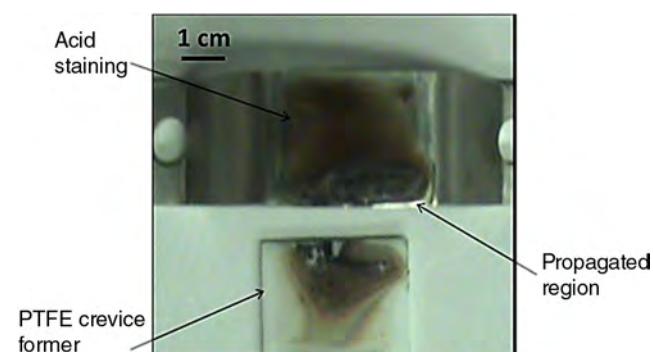


**FIGURE 4.** The surface of the N10362 alloy and the removed PTFE crevice former after crevice corrosion at 200  $\mu$ A and 150°C for 6 d.

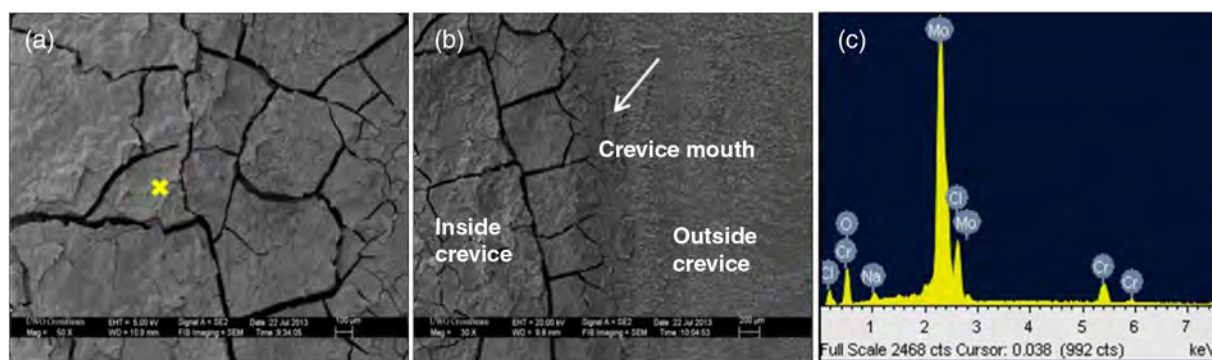


**FIGURE 5.** Corrosion morphology of the N10362 alloy (a) in the creviced region, (b) crevice mouth region, and (c) EDS analysis of the corrosion products at the location marked with an X.

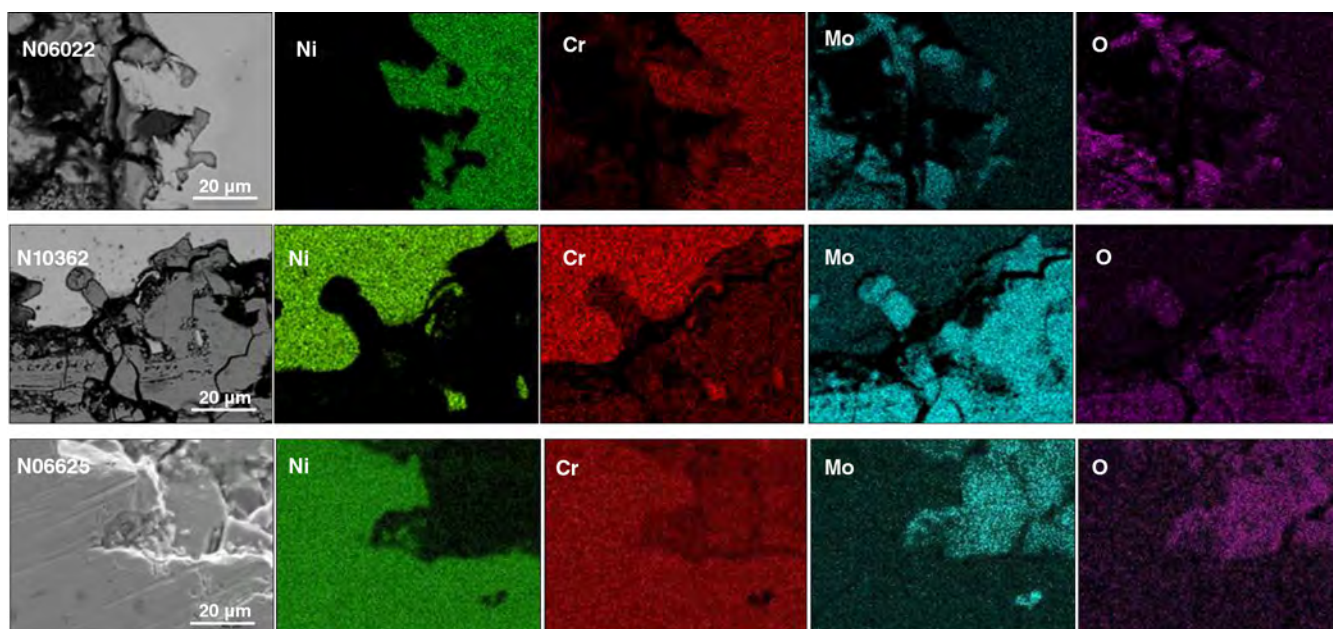


**FIGURE 6.** SEM images of the crevice corrosion fronts and the Ni, Cr, Mo, and O EDS maps on the surfaces of the N10362, N06022, and N06625 alloys. The EDS maps are on the same scale as the SEM images.

Figures 5(a) and (b) show the corrosion product deposit within the crevice and at the crevice mouth, respectively. The flaky product within the crevice indicated the formation of a hydrated layer, which dried and cracked on removal from the cell. Minimal deposition of corrosion product was observed outside the crevice mouth. Similar corrosion product morphology was observed on the N06022 and N06625 alloys for locations both inside and just outside the crevice. The EDS analysis (Figure 5(c)) shows that the dominant alloying element present in the deposit within the crevice was Mo.

Figure 6 shows SEM images and the corresponding EDS maps for Ni, Cr, Mo, and O for all three alloys after corrosion with an applied current of 200  $\mu$ A. The elemental analyses show similar trends for all three alloys. The signal intensities show that both Ni and Cr are depleted in the actively corroded areas, while Mo and O are enriched with respect to the base

metal composition, as expected based on the EDS spectrum in Figure 5(c). The intensity of the Mo signal recorded on the N10362 alloy, which has the highest Mo content, was 2.7 times more than that of the base metal, while this ratio was 2.6 and 2 for N06022 and N06625, respectively. For all three alloys, the enhanced signal for Mo in the actively corroded area is consistent with previous observations on the N06022 alloy.<sup>39,42</sup> The irregular corrosion front between the actively corroded area and the uncorroded alloy suggests that the propagation of this front is slightly enhanced along the grain boundaries in the alloy, particularly for the two high-Mo-containing (Mo + W for N06022) alloys.

Table 2 summarizes the EDS analyses of the crevice corroded areas on the three alloys after corrosion at 200  $\mu$ A. The values are the average of three measurements within each creviced area. For all three alloys, comparison of these results to the original

**TABLE 2**  
EDS Analyses of Corrosion Products (wt%)

Alloy/Elements	Ni	Cr	Mo	O	Na	Cl	W	Fe
UNS N06022	–	13.60	35.94	28.37	1.25	9.28	11.55	–
UNS N10362	–	5.07	60.23	23.33	1.11	8.79	–	–
UNS N06625	3.8	11.6	18.3	30.9	9.0	11.6	–	0.2

elemental content of the alloys (Table 1) confirms the common feature of Cr and Ni depletion and Mo enrichment (Mo + W for N06022). The high Cl and low Na signals reflect the ionic migration of Cl<sup>−</sup> ions into the creviced region to balance the positive charges created in the crevice by the oxidation half-reaction, and to compensate for the excess of anions outside the crevice resulting from oxygen reduction to hydroxide ions or water reduction to hydrogen and hydroxide ions on the counter electrode.<sup>39,43</sup>

ICP-MS analyses of the bulk electrolyte after crevice corrosion of the N06022 alloy detected 346 μg/L of Ni, 74.4 μg/L of Cr, and 16 μg/L of Mo (79.4%: 17%:3.6% Ni:Cr:Mo by wt.), confirming the dissolution and transport out of the crevice of Cr, and especially Ni, and the relative retention of Mo within the crevice. Although no analyses were performed for the other two alloys, similar active dissolution behavior would be expected. As EDS analyzes to a depth of a few micrometers, the small Ni signal detected for the N06625 alloy (Table 2) suggests that the Mo corrosion product layer may have been thinner on the creviced surface of this alloy.

### Distribution of Corrosion Damage

Figures 7 and 8 show the damaged areas within the crevice and a set of polished cross sections for all three alloys after crevice corrosion at 10 μA and 200 μA, respectively. The damaged areas are marked in red and the edge (mouth) of the crevice is defined by the white dashed lines. In all cases, only a single location within the crevice was corroded, and, with the exception of the crevice on N06625 propagated at 10 μA (Figure 7[a]), the damaged areas were all close to the edge (mouth) of the crevice, as expected. Using these damage maps and cross sections, crevice penetration depths and corroded surface areas were measured (Figures 7[g], 7[h], 8[g], and 8[h]). Because the penetration depths reported were measured as the deepest location on the single cross sections shown, they were not necessarily the maximum penetration depths within the entire damaged region.

The applied charge ( $Q_A$ ) in experiments using a current of 10 μA was 3.46 C on all three alloys and 103.68 C in the experiments with a current of 200 μA. The charge calculated from volume of material loss by corrosion is defined as  $Q_V$  and is calculated by Equation (1):

$$Q_V = \frac{\rho \times n \times F}{M} \times V \quad (1)$$

where M is the effective molar mass (the weighted average molar mass based on alloy composition), F is the Faraday constant, ρ is the density, n is the number of equivalent mols of electrons, and V is the corroded volume. The three alloys have similar densities (8.83 g/cm<sup>3</sup> [N10362], 8.69 g/cm<sup>3</sup> [N06022], and 8.44 g/cm<sup>3</sup> [N06625]) and the number of equivalents of electrons per mol of metal atoms involved in the corrosion reaction for all alloys is nearly identical, as they contain the same alloying elements. To estimate the volume of damage accumulated on the three alloys, the depth of the crevice was multiplied by the area corroded. As shown in Figures 7 and 8, at each of the applied currents, the corroded volumes (V) are effectively the same for all three alloys (~0.32 mm<sup>3</sup> [10 μA] and ~6 mm<sup>3</sup> [200 μA]), despite the 30-fold difference in total applied charge. This similarity indicates that  $Q_A$  is directly proportional to  $Q_V$ , with the alloys having similar  $Q_A/Q_V$  ratios at each applied current (within the error range of the crevice depth and surface area measurements).

An equivalent charge ( $Q_W$ ) can also be calculated from the weight change (W) resulting from corrosion using Equation (2):

$$Q_W = \frac{W \times n \times F}{M} \quad (2)$$

where W is the weight change due to corrosion. These  $Q_W$  values will be an underestimate because not all of the corrosion products accumulated in the grain boundaries could be removed. The ratio ( $Q_A/Q_W$ ) is a measure of the fraction of the corrosion driven by the external applied current. A value of  $Q_A/Q_W = 1$  would indicate all of the crevice corrosion was a result of the external applied current and none was supported by the reduction of protons in the extremely acidic crevice environment inside the crevice.

Three weight loss measurements were made on corroded N10362 crevices and converted to  $Q_W$  to estimate the  $Q_A/Q_W$  ratio. Each weight loss measurement was for an accumulated  $Q_A$  of 6.9 C and they yielded  $Q_A/Q_W$  ratios of 48.4%, 29.4%, and 22.6%. While variable, and bearing in mind that these  $Q_W$  values are underestimates, the  $Q_A/Q_W$  ratios indicate that ≥50% of the overall crevice damage was caused by proton reduction inside the crevice. This offers an explanation for the observed independence of  $E_C$  on applied current once the crevice is initiated (Figure 2).

Although the total volume of corrosion may be the same on each alloy, its distribution varies markedly

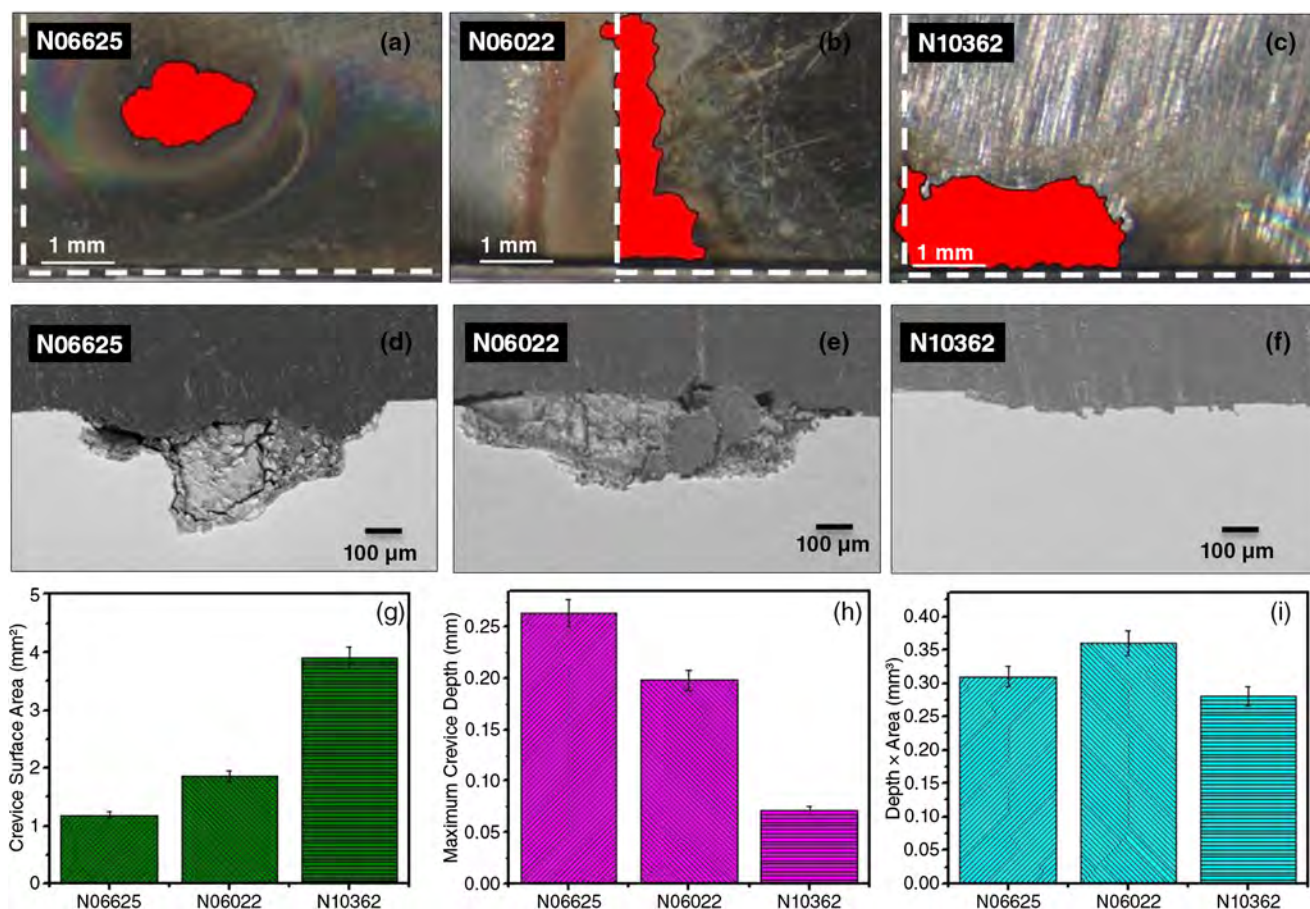
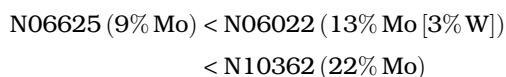


**FIGURE 7.** Alloy surfaces after crevice corrosion at an applied current of 10  $\mu\text{A}$  and an accumulated charge of 3.46 C. The top row shows optical images of the crevice-corroded surface areas of (a) N06625, (b) N06022, and (c) N10362 alloys. The corroded region is colored red. The dashed white lines in (a) through (c) show the edge of the creviced region as defined by the location of the crevice former. The middle row gives SEM images of crevice-corroded cross sections of (d) N06625, (e) N06022, and (f) N10362, and the bottom row plots (g) the maximum crevice depths, (h) crevice-corroded surface areas, and (i) crevice region volumes for the three alloys.

from alloy to alloy. As the Mo content of the alloy increases in the order:



the depth of penetration decreases, while the area corroded increases.

Figure 9 shows that the depth of crevice penetration decreases markedly as the Mo + W content of the corrosion products increases (W is present only in N06022 but is enriched like Mo within the crevice [Table 2] and known to exert an identical influence on crevice propagation<sup>34</sup>). Figure 10 shows the depth of penetration as a function of the Mo + W content of the original alloys (Table 1) for both applied currents. For a sufficiently high Mo + W content, the penetration depth is only marginally dependent on the applied current, confirming that the dominant factor controlling active propagation is the chemical influence of

Mo + W. By contrast, the depth of penetration on the N06625 alloy increases markedly when the applied current is increased, a strong indication that active propagation is still mainly controlled by the cathodic reaction proceeding outside the crevice, which could reflect a higher  $Q_A/Q_W$  ratio, although this remains to be demonstrated.

The damage maps in Figures 7 and 8 show that, besides the total area actively corroded, the lateral dimensions of damage propagation also vary with the alloy composition. This is particularly noticeable for the N06022 and N10362 alloys. For both alloys, propagation follows the edge of the crevice, but there is a more marked tendency for propagation toward the center of the crevice on N10362 than on N06022. While observable in experiments with an applied current of 200  $\mu\text{A}$  (Figures 8[b] and [c]), it is more obvious in experiments at the lower current (10  $\mu\text{A}$ ) (Figures 7[b] and [c]). This ability to propagate more deeply into the crevice could reflect the lower Cr content of the N10362 compared to N06022; i.e., it is kinetically easier to activate areas at

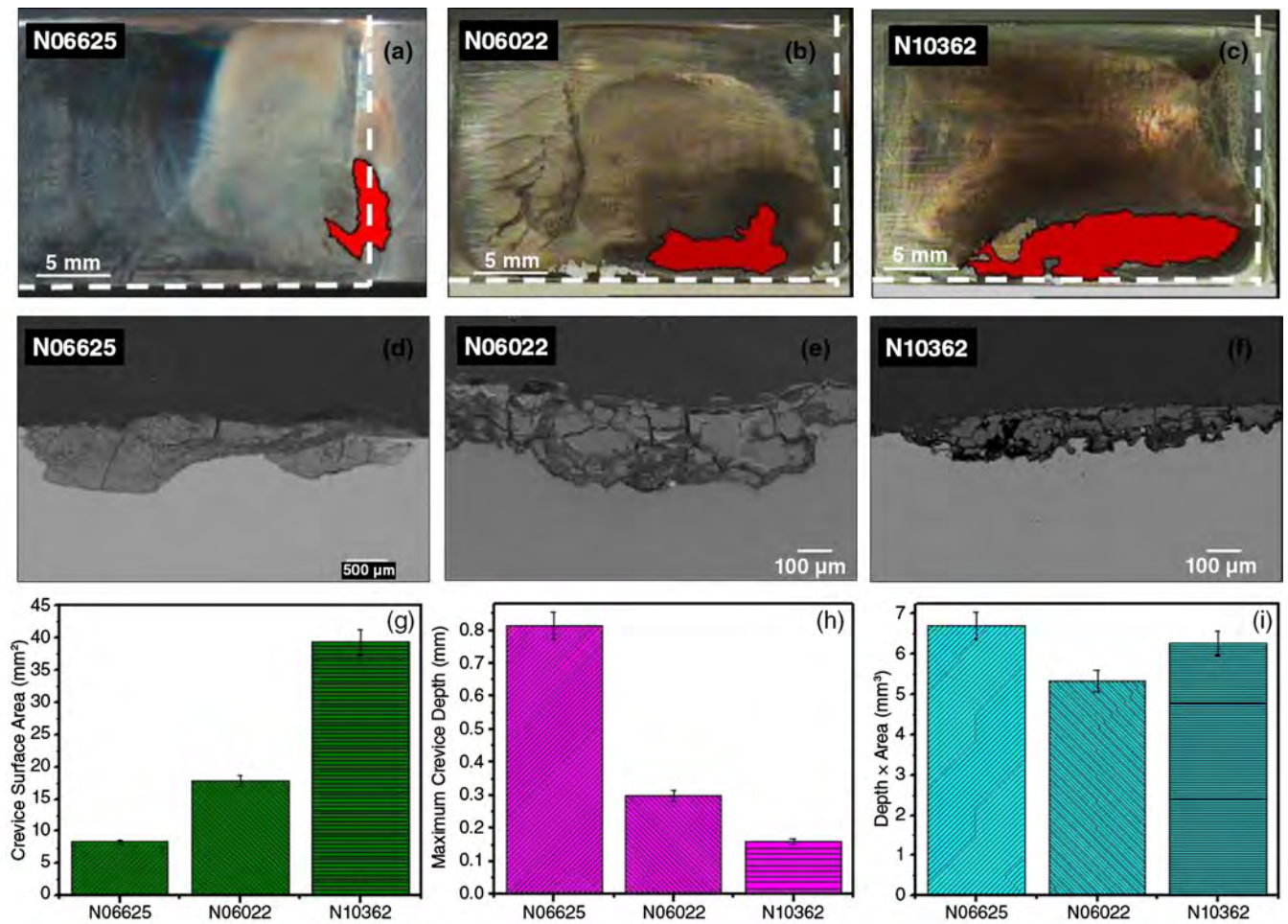


**FIGURE 8.** Alloy surfaces after crevice corrosion at an applied current of 200  $\mu\text{A}$  and an accumulated charge of 103.68 C. The top row shows optical images of the crevice-corroded surface areas of (a) N06625, (b) N06022, and (c) N10362 alloys. The corroded region is colored red. The dashed white lines in (a) through (c) show the edge of the creviced region as defined by the location of the crevice former. The middle row gives SEM images of crevice-corroded cross sections of (d) N06625, (e) N06022, and (f) N10362, and the bottom row plots (g) the maximum crevice depths, (h) crevice-corroded surface areas, and (i) crevice region volumes for the three alloys.

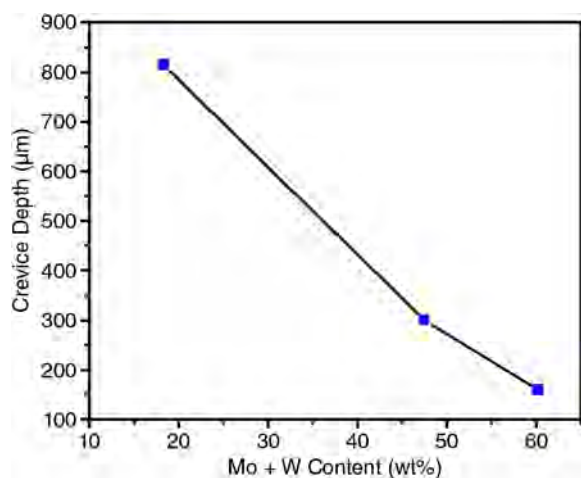


**FIGURE 9.** The crevice depth in experiments at 200  $\mu\text{A}$  vs. the content of Mo + W in the corrosion products (Table 2).

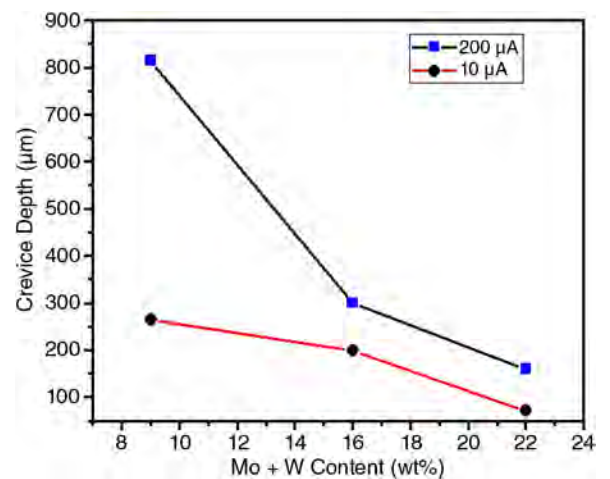


**FIGURE 10.** The crevice depth for experiments at both applied currents as a function of the Mo + W content in the uncorroded alloys (Table 1).

deeper locations on N10362. As discussed, the results in Figure 2 show that activation involves a competition between breaching the Cr(III) oxide barrier layer and the tendency to repassivate the breakdown site by the accumulation of molybdate and tungstate deposits, and that activation is more readily achieved on the low-Cr-containing N10362. An explanation for this effect in terms of the potential distribution within the crevice (i.e., according to the IR drop model<sup>38,44</sup>) is not so readily constructed, indicating that chemical effects are dominant in determining crevice corrosion behavior on these alloys at these enforced propagation rates.

### Discussion: Chemistry in Crevice-Corroded Regions

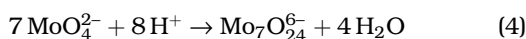
The local chemistry within the active crevice is clearly a key feature in controlling the activation of corrosion and the propagation of the accumulated damage. The pH in active locations could approach zero.<sup>20,45</sup> Potential-pH diagrams for the three key elements (Ni, Cr, and Mo), calculated for 4 M NaCl (at 120°C) show that both Cr<sub>2</sub>O<sub>3</sub> and NiO are unstable at pH < 3. Cation solubility is increased by the formation of chloride complexes (e.g., CrCl<sup>2+</sup>, NiCl<sup>+</sup>). Thus, the loss of Cr and Ni as soluble species from the creviced area, detected by solution analyses and indicated by their absence from the corrosion products deposited within the crevice, is not surprising. The redeposition of Cr, as Cr(OH)<sub>3</sub> or Cr<sub>2</sub>O<sub>3</sub>, at the higher pH values prevailing outside the crevice would be expected.<sup>42</sup>

The role of Mo in controlling the active corrosion within a propagating crevice has been previously investigated,<sup>32-34</sup> and the accumulation of Mo(VI) as polymeric species such as Mo<sub>8</sub>O<sub>4</sub><sup>6-</sup> (and possibly also as Mo<sub>7</sub>O<sub>24</sub><sup>6-</sup> and Mo<sub>3</sub>O<sub>10</sub><sup>2-</sup>) demonstrated using Raman spectroscopy.<sup>34</sup> Although undetected in this Raman analysis,<sup>34</sup> W is expected to accumulate as polymeric tungstates also.

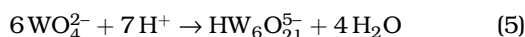
The initial dissolution of Mo within an activating crevice will be as MoO<sub>4</sub><sup>2-</sup>:



but even for pH values slightly <6.5, paramolybdate species are known to form via proton-consuming reactions<sup>46-47</sup> such as:



Similar reactions are anticipated for W:<sup>43,46</sup>



supporting the authors' argument that W will exert an influence similar to that of Mo within an active crevice. It was previously suggested<sup>34</sup> that the ability of Mo (and W) to suppress crevice propagation can be attributed to

this tendency to polymerize, with the extent of polymerization, and hence proton consumption, increasing markedly as the pH decreases:



Under the constant current conditions used in the authors' experiments, metal dissolution will be on-going at a constant rate. Because this rate is the same (at the same current) irrespective of the alloy composition, the rate of production of dissolved metal species will be constant, leading to the on-going production of acidic conditions by cation hydrolysis processes, particularly for Cr, Mo, and W, e.g.:



Although some of the protons produced by these reactions will be consumed by the polymerization reactions, the modification of the local pH by molybdate formation will not be as significant as suggested previously.<sup>8,48</sup> Each mol of Mo will, at best, neutralize 1.5 mols of H<sup>+</sup> (Equation [6]), while the hydrolysis of 1 mol of Mo<sup>6+</sup> leads to the formation of 8 H<sup>+</sup> (Equation [7]). In addition, the hydrolysis of other alloy elements, such as Cr and W (for N06022 alloy), will also produce H<sup>+</sup>, eight in the case of Cr<sup>6+</sup> (Equation [8]). Thus, the production of H<sup>+</sup> will far exceed its consumption by molybdate formation, and polymerization will have little effect on the pH. The more likely influence of molybdate formation is that it stifles active alloy dissolution by formation of a protective layer. The more rapid production of large amounts of soluble Mo(VI) for the high-Mo-containing alloy (N10362) compared to the low-Mo-containing alloys (N06022 and N06625) would then lead to the more rapid blockage of active sites. The analyses in Table 2 show that the Mo content of the corrosion product deposit increased with the Mo content of the alloy. However, whether this reflects a higher Mo content of the polymeric layer or a thicker molybdate layer is uncertain.

Irrespective of which of these is the case, the correlation between the Mo content of the corrosion product and the depth of penetration confirms the ability of such a layer to stifle active dissolution. Because repassivation is prevented under constant current conditions, this local site suppression leads to the lateral spread of propagation, as previously described for N06022,<sup>34</sup> a process that requires the on-going activation of new sites. This is sustained by the concentration of current around the periphery of the expanding damage area.

## CONCLUSIONS

❖ The effects of the alloying elements Cr, Mo, and W on crevice corrosion initiation and propagation on

three commercial Ni alloys were investigated under galvanostatic control in 3 M NaCl at 150°C. The galvanostatic approach was used to study activation and propagation by avoiding repassivation.

- ❖ The activation step was shown to depend on the Mo content of the alloy and to involve competition between Cr(III) barrier layer breakdown and Mo(VI)/W(VI) accumulation to repair breakdown sites.
- ❖ Under stable propagation conditions, the  $E_C$  measured is proportional to the Mo + W content of the alloy, and almost constant and independent of the applied anodic current, indicating that propagation is controlled by the crevice chemistry.
- ❖ Mo content determines the distribution of corrosion damage. For N06625 (9% Mo) propagation leads predominantly to penetration into the alloy, whereas increased Mo content (N06022 [13 wt%] and N10362 [22 wt%]) causes corrosion damage to spread laterally across the creviced surface. This is attributed to formation of polymeric molybdates, which occurs more rapidly as the Mo content increases, and limits the depth of penetration into the alloy.
- ❖ The primary influence of Mo is to stifle the dissolution of the alloy by accumulation at active sites. Its influence on controlling pH within the crevice is minor.
- ❖ Greater than 50% of propagation is caused by proton reduction inside the crevice.

## ACKNOWLEDGMENTS

The authors would like to thank Haynes International (Kokomo, Indiana) for their generous donation of material and the Western Nanofabrication Facility for SEM and EDS analyses. This project received funding from the Natural Sciences and Engineering Research Council of Canada (NSERC).

## REFERENCES

1. R.W. Revie, H.H. Uhlig, *Uhlig's Corrosion Handbook*, 3rd ed. (Hoboken, NJ: John Wiley & Sons, 2011).
2. J.C. Estill, K.J. King, D.V. Fix, D.G. Spurlock, G.A. Hust, S.R. Gordon, R.D. McCright, R.B. Rebak, G.M. Gordon, "Susceptibility of Alloy 22 to Environmentally Assisted Cracking in Yucca Mountain Relevant Environments," Dept. of Energy, UCRL-JC-145992, January 2002.
3. R.M. Carranza, M.A. Rodríguez, R.B. Rebak, *Corrosion* 63 (2007): p. 480-490.
4. M.A. Rodríguez, R.M. Carranza, R.B. Rebak, *Metall. Mater. Trans. A* 36 (2005): p. 1179-1185.
5. R.M. Carranza, C.M. Giordano, M.A. Rodríguez, R.B. Rebak, "Effect of the Addition of Organic Acids to the General and Crevice Corrosion Behavior of Alloy 22 in Chloride Solutions," CORROSION 2008, paper no. 578 (Houston, TX: NACE International, 2008).
6. E.C. Hornus, C. Mabel Giordano, M.A. Rodríguez, R.M. Carranza, *MRS Online Proceedings Library* 1475 (2012): p. 251-258.
7. E.C. Hornus, C.M. Giordano, M.A. Rodríguez, R.M. Carranza, R.B. Rebak, "Effect of Temperature on Crevice Corrosion Susceptibility of Nickel Alloys for Nuclear Repositories," CORROSION 2013, paper no. 2504 (Houston, TX: NACE, 2013).
8. J.R. Hayes, J.J. Gray, A.W. Szmody, C.A. Orme, *Corrosion* 62 (2006): p. 491-500.
9. F. Wong, R. Buchheit, *ECS Trans.* 16 (2009): p. 91-100.
10. X. Shan, J.H. Payer, *J. Electrochem. Soc.* 156 (2009): p. C313-C321.
11. A.C. Lloyd, J.J. Noël, S. McIntyre, D.W. Shoesmith, *Electrochim. Acta* 49 (2004): p. 3015-3027.
12. A.C. Lloyd, D.W. Shoesmith, N.S. McIntyre, J.J. Noël, *J. Electrochem. Soc.* 150 (2003): p. B120-B130.
13. P. Marcus, J.M. Grimal, *Corros. Sci.* 33 (1992): p. 805-814.
14. S. Haupt, H.H. Strehblow, *Corros. Sci.* 37 (1995): p. 43-54.
15. C.O.A. Olsson, D. Landolt, *Electrochim. Acta* 48 (2003): p. 1093-1104.
16. K. Sieradzki, R.C. Newman, *J. Electrochem. Soc.* 133 (1986): p. 1979-1980.
17. P. Marcus, *Electrochim. Acta* 43 (1998): p. 109-118.
18. A.C. Lloyd, J.J. Noël, N.S. McIntyre, D.W. Shoesmith, *JOM* 57 (2005): p. 31-35.
19. B.A. Kehler, J.R. Scully, *Corrosion* 61 (2005): p. 665-684.
20. B.A. Kehler, G.O. Ilevbare, J.R. Scully, *Corrosion* 57 (2001): p. 1042-1065.
21. R.S. Lillard, M.P. Jurinski, J.R. Scully, *Corrosion* 50 (1994): p. 251-265.
22. S. Haudet, M.A. Rodríguez, R.M. Carranza, "Effect of Alloy Composition on the Localized Corrosion Resistance of Nickel Alloys," in *Scientific Basis for Nuclear Waste Management XXXV*, eds. R.M. Carranza, G.S. Duffó, R.B. Rebak, MRS Symposium Proceedings, vol. 1475 (New York, NY: Cambridge University Press, 2012), p. 489-494.
23. F. Bocher, R. Huang, J.R. Scully, *Corrosion* 66 (2010): p. 55002-55015.
24. S. Haudet, M. Rodríguez, R.M. Carranza, R.B. Rebak, "Effect of Alloy Composition on the Crevice Corrosion Resistance of Nickel Alloys," CORROSION 2012, paper no. 1455 (Houston, TX: NACE, 2012).
25. P. Kritzer, N. Boukis, E. Dinjus, *Corrosion* 56 (2000): p. 265-272.
26. A.K. Mishra, D.W. Shoesmith, *Corrosion* 70 (2014): p. 721-730.
27. A.K. Mishra, D.W. Shoesmith, *Electrochim. Acta* 102 (2013): p. 328-335.
28. P. Jakupi, D. Zagidulin, J.J. Noël, D.W. Shoesmith, *Electrochim. Acta* 56 (2011): p. 6251-6259.
29. D. Zagidulin, X. Zhang, J. Zhou, J.J. Noël, D.W. Shoesmith, *Surf. Interface Anal.* 45 (2013): p. 1014-1019.
30. X. Zhang, D. Zagidulin, D.W. Shoesmith, *Electrochim. Acta* 89 (2013): p. 814-822.
31. X. Zhang, D.W. Shoesmith, *Corros. Sci.* 76 (2013): p. 424-431.
32. P. Jakupi, J.J. Noël, D.W. Shoesmith, *Corros. Sci.* 54 (2012): p. 260-269.
33. P. Jakupi, J.J. Noël, D.W. Shoesmith, *Corros. Sci.* 53 (2011): p. 3122-3130.
34. P. Jakupi, F. Wang, J.J. Noël, D.W. Shoesmith, *Corros. Sci.* 53 (2011): p. 1670-1679.
35. X. He, J.J. Noël, D.W. Shoesmith, *J. Electrochem. Soc.* 149 (2002): p. B440-B449.
36. J. Oldfield, W. Sutton, *Br. Corros. J.* 13 (1978): p. 13-22.
37. J. Oldfield, W. Sutton, *Br. Corros. J.* 13 (1978): p. 104-111.
38. H.W. Pickering, *Corrosion* 42 (1986): p. 125-140.
39. P. Jakupi, D. Zagidulin, J. Noël, D.W. Shoesmith, *ECS Trans.* 3 (2007): p. 259-271.
40. N. Ebrahimi, M.H. Moayed, A. Davoodi, *Corros. Sci.* 53 (2011): p. 1278-1287.
41. D. Shoesmith, J. Noel, D. Hardie, B. Ikeda, *Corros. Rev.* 18 (2000): p. 331-360.
42. R.G. Kelly, K.C. Stewart, "Combining the Ohmic Drop and Critical Crevice Solution Approaches to Rationalize Intermediate Attack in Crevice Corrosion," in *Passivity of Metals and Semiconductors VIII*, eds. M.B. Ives, B.R. MacDougall, J.A. Bardwell, PV 99-42 (Pennington, NJ: The Electrochemical Society, 2001).
43. K.Y.S. Ng, E. Gulari, *Polyhedron* 3 (1984): p. 1001-1011.
44. H.W. Pickering, *J. Electrochem. Soc.* 150 (2003): p. K1-K13.
45. B.K. Nash, R.G. Kelly, *Corros. Sci.* 35 (1993): p. 817-825.
46. C. Heitner-Wirguin, R. Cohen, *J. Inorg. Nucl. Chem.* 26 (1964): p. 161-166.
47. C.F. Baes, R.E. Mesmer, *The Hydrolysis of Cations* (New York, NY: Wiley, 1976).
48. R.S. Lillard, M.P. Jurinski, J.R. Scully, *Corrosion* 50 (1994): p. 251-265.